A generalized interface reaction kinetic model for describing heterogeneous processes driven by contracting mechanisms

Juan Arcenegui-Troya[1] · Pedro E. Sánchez-Jiménez[2,3] · María del Rocío Rodríguez-Laguna[2,4] · Antonio Perejón[2,3] · Luis A. Pérez-Maqueda[2]

Abstract

The correct determination of the kinetic model and the kinetic parameters that describe a heterogeneous process is key to accurately predicting its progress within a wide range of conditions, which is one of the main purposes of kinetic analysis. Albeit ideal kinetic models continue to be used to gain insight about the process mechanism, they are constrained by certain assumptions that are rarely met in real experiments and limit their applicability. This is the case of contracting (or interface) kinetic models, which are one of the most commonly used. Thus, the ideal kinetic model $R2$ is derived by assuming a cylindrical contraction in the radial direction but not contemplating the possibility of a contraction in the direction of the axis of the cylinder. Moreover, in the case of the ideal model $R3$, it is assumed that contraction takes place simultaneously in particles of identical dimensions in all three directions of space (spheres or cubes). Here, it is revisited this type of model, and it is considered the contraction of particles with different geometries, namely cylinders with different aspect ratios and rectangular cuboids. Besides, a novel generalized interface reaction model is proposed, which covers all the studied cases and broadens the range of applicability to more complex situations involving different geometries and inhomogeneous particle sizes. Finally, the proposed model is applied to the analysis of the experimental thermal dissociation of ammonium nitrate, previously described in the literature as a sublimation process. It is proved that the novel kinetic model provides a more accurate description of the kinetics of the reaction and better prediction capabilities.

✉ Juan Arcenegui-Troya
  jjarcenegui@uloyola.es

✉ Luis A. Pérez-Maqueda
  maqueda@icmse.csic.es

1 Department of Engineering, Universidad Loyola Andalucía, Avda. de las Universidades s/n, 41704 Dos Hermanas, Seville, Spain

2 Instituto de Ciencia de Materiales de Sevilla, C. S. I. C.-Universidad de Sevilla, C. Américo Vespucio no 49, 41092 Seville, Spain

3 Departamento de Química Inorgánica, Facultad de Química, Universidad de Sevilla, 41012 Seville, Spain

4 Present Address: Advanced Technology of Molten Salts Department, Idaho National Laboratory, Idaho Falls, ID 83415, USA

Introduction

The kinetic analysis of heterogeneous processes is a powerful tool applied for studying a myriad of processes. For instance, kinetic analysis has been applied to biomass energy production [1], thermochemical energy storage [2], food processing [3], polymer curing [4–8] and decomposition [9–12], hydration and dehydration [13–15], pyrolysis [16], sintering [17–19], crystallization [20–23], etc. Its success lies in its capability to provide useful information that can be employed for predicting the progress of a process in a wide range of operating conditions, including those that cannot be reached under laboratory experimental conditions.

The general equation for heterogeneous kinetics [24–26] can be written in its differential form as follows:

$$\frac{d\alpha}{dt} = A \exp\left(-E/RT\right) f(\alpha) \tag{1}$$

And in its integral form as follows:

$$g(\alpha) = \int \frac{1}{f(\alpha)} d\alpha = \int_0^t A \exp\left(-\frac{E}{RT}\right) dt = kt \qquad (2)$$

where α is the converted fraction, A is the pre-exponential factor, E is the apparent activation energy, T is the temperature, k is the rate constant, and $f(\alpha)$ and $g(\alpha)$ are mathematical functions corresponding to the kinetic model describing the geometrical progress of the reacted volume in its differential and integral forms, respectively. One of the families of ideal kinetic models most commonly used in literature for describing heterogeneous processes is the contracting kinetic models, also known as interface models. Many different processes such as the thermal decomposition of limestone [27], the dehydration of salt hydrates [28], the thermal dissociation of ammonium nitrate [29] or the thermal decomposition of novel 2D materials [30, 31] have been defined in terms of these kinetic models. These models assume that reaction starts on the particle surface, and reaction rate is determined by the advancement of the interface inside the particles. Depending on the shape of the particles, different kinetic models are derived. Thus, $R2$ model is derived for cylindrical particles, $R3$ for spherical (or cubic) particles and $F0$ for unidirectional contraction with constant surface area. For the derivation of all these models, it is assumed that all particles are identical in shape and size. Previous studies have reported that the inhomogeneity in particle size strongly affects the shape of $f(\alpha)$ [32]. Thus, the particle size distribution (PSD) influences the kinetics in such a way that a process obeying an interface reaction mechanism may even seem driven by a diffusion-controlled kinetic model [33]. Moreover, ignoring aspects related to the geometry of the particles might lead to erroneous conclusions when using ideal kinetic models from the literature to fit experimental data. Some authors have proposed using semi-empirical equations [34–38], but these models are used just as fitting equations that do not provide any physical meaning.

In this work, the interface kinetic models are revisited and new models for more realistic conditions are defined,

including a model for cylindrical particles and two directions reaction progress, and a model for rectangular cuboidal particles and three directions reaction progress. Furthermore, a generalized kinetic model for contraction of bodies with different geometries is proposed, which covers, not only conventional models such as $R2$, $R3$ and $F0$, but other more complex geometries and particle size distributions. Finally, the model has been validated with a real case: the kinetics of the thermal dissociation of ammonium nitrate.

Theoretical foundation

Standard interface ideal kinetic models proposed in literature: *R*2, *R*3 and *F*0

Ideal interface kinetic models are proposed by assuming quite simplistic conditions. Thus, in the case of the $R2$ kinetic model, illustrated in Fig. 1 (left), the cylindrical interface that separates the reacted volume from the unreacted volume contracts radially according to [39]:

$$r = r_0 - k't \qquad (3)$$

where r and r_0 are the radius interfaces at the instants t and $t = 0$, and k' represents the rate of contraction, which obeys an Arrhenius-type relationship with temperature. In this case, the converted fraction can be expressed as follows:
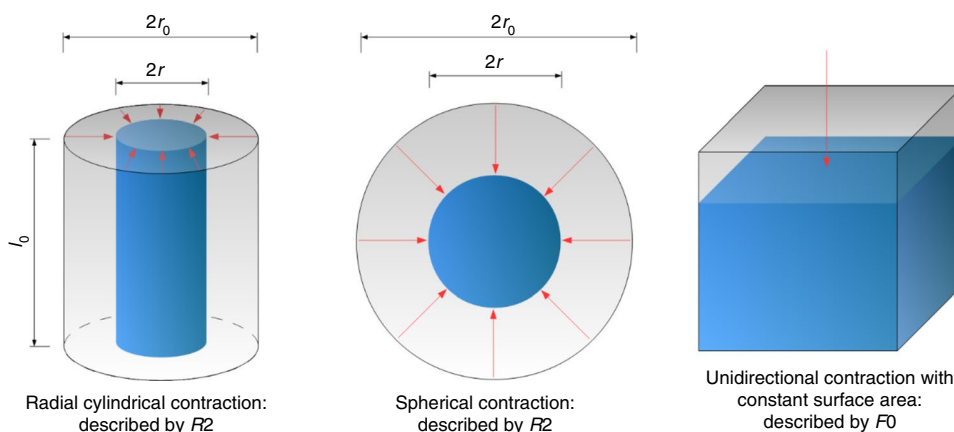
$$\alpha = 1 - (1 - kt)^2 \qquad (4)$$

or

$$g(\alpha) = 1 - (1 - \alpha)^{\frac{1}{2}} = kt \qquad (5)$$

where $k = k'/r_0$ is the rate constant. The fact that k depends on the radius of the particles explains why the PSD plays a relevant role in the kinetics of a sample that reacts according to a contracting area model [32]. The kinetic model $R2$ is

Fig. 1 Schematic illustration of interface reaction standard kinetic models for cylindrical (*R*2, left), spherical (*R*3, center) and unidirectional (*F*0, right) contraction

Radial cylindrical contraction: described by *R*2

Spherical contraction: described by *R*2

Unidirectional contraction with constant surface area: described by *F*0

applicable as long as the cylinder is much longer than wider. Nonetheless, since it does not consider the possibility of contraction in the direction of the cylinder axis, it cannot be applied to situations in which both dimensions, height and radius, are comparable and the cylinder contracts both radially and longitudinally.

In the case of the $R3$ kinetic model, shown in Fig. 1 (center), corresponding to the contraction of a sphere (or a cube), the converted fraction could be described, following the same procedure shown above, as follows:

$$\alpha = 1 - (1 - kt)^3 \tag{6}$$

or

$$g(\alpha) = 1 - (1 - \alpha)^{\frac{1}{3}} = kt \tag{7}$$

The $R3$ kinetic model is applicable only for a perfect sphere (or cube) that is not distorted in any direction.

The zero-order kinetic model ($F0$) might be interpreted as a unidirectional contraction with constant surface area as shown in Fig. 1 (right). In this case, the converted fraction could be described by the following equation:

$$g(\alpha) = \alpha = kt \tag{8}$$

Novel interface kinetic model for cylindrical particles and two directions reaction progress

As mentioned in the previous section, in the proposal of the $R2$ kinetic model, it is assumed that the process advances only radially. Here, it will be considered a more realistic situation where the process progresses in both directions. Thus, for a cylindrical particle of radius r_0, height l_0 and density ρ_0 (see Fig. 2, left), the initial mass of the particle can be expressed in terms of these parameters as follows:

$$m_0 = \rho_0 \pi r_0{}^2 l_0 \tag{9}$$

If the particle undergoes a process in which the transformation rate is proportional to the surface of the interface, separating reacted (in purple in Fig. 2 on the right)
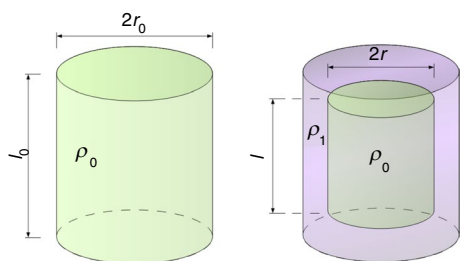
and unreacted parts (in green), the process rate can be expressed as follows:

$$\frac{dm}{dt} = -C(2\pi r l + 2\pi r^2) \tag{10}$$

where r and l are the radius and the height, respectively, of the interface that separates the fractions converted and unconverted, and C the proportionality constant. The mass of the particle at the time t is given by:

$$m(t) = \rho_1 \pi r_0^2 l_0 + (\rho_0 - \rho_1)\pi r^2 l \tag{11}$$

Being ρ_1 the density of the converted volume. Thus, the derivative can be expressed as follows:

$$\frac{dm}{dt} = (\rho_0 - \rho_1)\pi \left(2rl\frac{dr}{dt} + r^2\frac{dl}{dt} \right) \tag{12}$$

By combining Eqs. (10), (11) and (12), it follows:

$$\left(2rl\frac{dr}{dt} + r^2\frac{dl}{dt} \right) = -\frac{2C}{(\rho_0 - \rho_1)}(rl + r^2) \tag{13}$$

Equation (13) only admits as solutions:

$$\frac{dr}{dt} = -k' \tag{14}$$

$$\frac{dl}{dt} = -2k' \tag{15}$$

Being $k' = C/(\rho_0 - \rho_1)$. It should be noted that a factor of two must be incorporated to align the rate of height contraction with Eq. (13). Therefore, integrating Eqs. (14) and (15) and taking into account the initial conditions, it follows:

$$r = r_0 - k't \tag{16}$$

$$l = l_0 - 2k't \tag{17}$$

Then, by substituting the expressions for r (Eq. 16) and l (Eq. 17) into Eq. (11), the mass of the cylindrical particle can be defined as a function of time:

$$m(t) = \rho_1 \pi r_0^2 l_0 + (\rho_0 - \rho_1)\pi (r_0 - k't)^2 (l_0 - 2k't) \tag{18}$$

Consequently, the converted fraction can be calculated as follows:

$$\alpha(t) = 1 - \frac{(r_0 - k't)^2 (l_0 - 2k't)}{r_0^2 l_0} \tag{19}$$

Introducing the aspect ratio defined as $\varepsilon = l_0/2r_0$, Eq. (19) becomes:

Fig. 2 Schematic illustration of the bidirectional contraction model for a cylinder

$$\alpha(t) = 1 - (1 - kt)^2 \left(1 - \frac{k}{\varepsilon}t\right) \tag{20}$$

With $k = k'/r_0$. Note that Eq. (20) reduces to Eq. (4) (corresponding to the $R2$ model) when $\varepsilon \to \infty$, that is when the contraction takes place only in the radial direction of the cylinder. Furthermore, for $\varepsilon = 1$, the converted fraction evolves according to the kinetic model $R3$ (Eq. 6). Furthermore, Eq. (20) shows that the process progresses toward the inner of the particle while the interface that separates the converted material from that unreacted one contracts radially at rate k and longitudinally at rate k/ε.
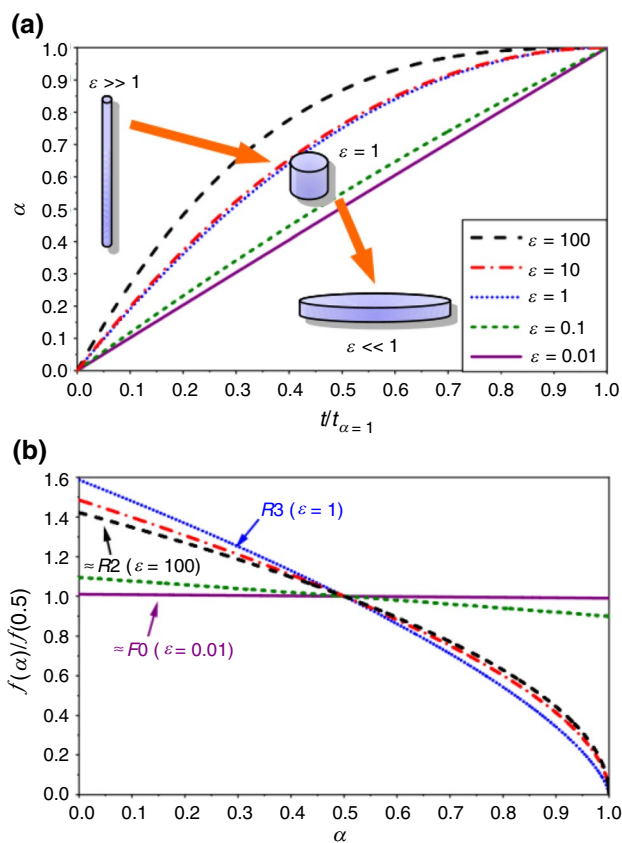
Figure 3a shows α as a function of the time normalized with the interval needed to attain the full conversion ($\alpha = 1$) for different aspect ratio (ε) values. Albeit it does not affect the plot, the rate constant was set at $k = 1$ for the six presented curves. It might be observed in Fig. 3a that as ε decreases, the time evolution of α tends to a straight line, which is equivalent to a zero-order ($F0$) kinetic model, $f(\alpha) = 1$, corresponding with a process where the surface

(a)

(b)

Fig. 3 a Converted fraction as a function of the time normalized with the interval needed for the process completion (normalized process time), for several values of ε. **b** Normalized kinetic model and comparison with the zero-order ($F0$), the contracting area ($R2$) and the contracting volume ($R3$) models. The simulations were conducted setting $k = 1$

remains constant (for example for the vaporization of a liquid). This is consistent with what it is expected taking into account that when $\varepsilon \ll 1$ the contracting rate in the longitudinal direction is much larger than that accounting for the radial contraction (i.e., $k/\varepsilon \gg k$, for $\varepsilon \ll 1$). Consequently, while the particle completely contracts in the longitudinal direction, its radius and, hence, its surface ($\sim 2\pi r^2$ for $\varepsilon \ll 1$) remains almost constant during the entire process, as in the case described by the $F0$ kinetic model. Moreover, as ε increases, the shape of the curves resembles, as expected, the contracting area $R2$ kinetic model. In this latter case, the contraction mainly occurs radially, while the particle length remains approximately constant.

The relationship between the parameter ε and the kinetic model can be more clearly seen in Fig. 3b, where the kinetic model obtained in each case, normalized to their values for $\alpha = 0.5$, have been plotted. The normalized kinetic model has been calculated as follows: according to Eq. (1), under isothermal ($T = $ constant) conditions, the kinetic model is proportional to the derivative: $d\alpha/dt = kf(\alpha)$, being k the proportionality constant. Therefore, by dividing $d\alpha/dt$, calculated by differentiation of Eq. (20), between the value of the derivative for $\alpha = 0.5$, the normalized kinetic model can be obtained:

$$\frac{\frac{d\alpha}{dt}}{\frac{d\alpha}{dt}\Big|_{\alpha=0.5}} = \frac{f(\alpha)}{f(\alpha = 0.5)} \tag{21}$$

In the limits, the kinetic models obtained are $F0$ and $R2$, which correspond to $\varepsilon = 0$ and $\varepsilon \to \infty$, respectively, while for $\varepsilon = 0$ it yields the $R3$ kinetic model (Fig. 3b).
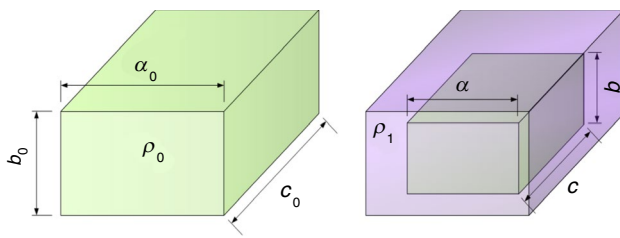
Novel interface kinetic model for rectangular cuboidal particles and three directions reaction progress

As mentioned in the introduction section, the $R3$ interface kinetic model assumes either a cube or a sphere where the process progresses in three dimensions at the same rate. A more general situation will be a rectangular cuboid with edges a, b and c, as shown in Fig. 4.

By applying in this case, the same reasoning used for the cylinder in Sect. "Novel interface kinetic model for cylindrical particles and two directions reaction progress", the following expression is obtained for the converted fraction as a function of time:

$$\alpha(t) = 1 - \left(1 - \frac{k''}{a_0}t\right)\left(1 - \frac{k''}{b_0}t\right)\left(1 - \frac{k''}{c_0}t\right) \tag{22}$$

In the particular case, when all dimensions of the cuboid are identical (a cube): $a_0 = b_0 = c_0$, Eq. (22) turns into:

Fig. 4 Schematic illustration of the interface kinetic model for rectangular cuboidal particles and three directions reaction progress

$$\alpha(t) = 1 - \left(1 - \frac{k''}{a_0} t \right)^3 \tag{23}$$

That corresponds to the 3-D interface reaction model $R3$. Moreover, in the case that two edges are equal and one is different, $a_0 = b_0 \neq c_0$, Eq. (22) reduces to Eq. (20) by simply redefining the constants: $k = k''/a_0$ and $\varepsilon = c_0/a_0$, which corresponds to the case of the model presented in Sect. "Novel interface kinetic model for cylindrical particles and two directions reaction progress" for cylindrical particles and two directions reaction progress. Therefore, Eq. (22) shows a general expression that covers all interface kinetic models.

Figure 5a, b shows, as a way of example, the time evolution of the converted fraction and the normalized kinetic model, respectively, for a rectangular cuboid with edges $a_0 = 0.1$ μm, $b_0 = 0.5$ μm and $c_0 = 2$ μm, simulated assuming $k''=10^{-4}$ μm s^{-1}.

Generalized semi-empirical interface reaction kinetic model

The two novel kinetic models proposed in Sect. "Novel interface kinetic model for cylindrical particles and two directions reaction progress" (Eq. 20) and in Sect. "Novel interface kinetic model for rectangular cuboidal particles and three directions reaction progress" (Eq. 22) are an advanced approach for interface reaction kinetic models that consider the progress of the process in different directions of the space for asymmetrical particles. Nevertheless, the $f(\alpha)$ function cannot be directly derived from Eqs. (20) and (22) for these two models.

In this section, it is proposed a generalized semi-empirical equation that fits not only Eqs. (20) and (22) for any values of ε or a_0, b_0 and c_0, but that also fits conventional interface growth models and their deviations due to, for example, particle size distribution.

Standard empirical models, such as the Sestak–Berggren equation, $f(\alpha) = c\alpha^m (1 - \alpha)^n (-\ln(1 - \alpha))^p$, and the n-order reaction kinetic model, $f(\alpha) = A(1 - \alpha)^n$, fail to fit the two
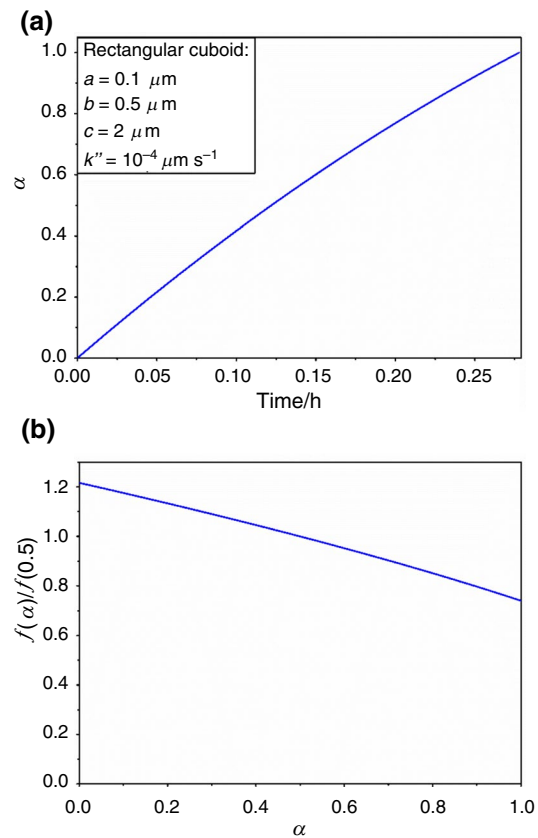

Fig. 5 a Time evolution of the converted fraction during the contraction of a regular cuboid with edges $a_0 = 0.1$ μm, $b_0 = 0.5$ μm and $c_0 = 2$ μm. **b** Normalized kinetic model. The simulations were conducted setting $k'' = 10^{-4}$ μm s^{-1}

newly proposed interface models for different values of ε and combinations of a_0, b_0 and c_0. As a way of example, Fig. 6a shows the best fit of both the Sestak–Berggren and n-order models, to data plotted in Fig. 5b, corresponding to a cuboid with edges $a_0 = 0.1$ μm, $b_0 = 0.5$ μm and $c_0 = 2$ μm and $k'' = 10^{-4}$ μm s^{-1}. As might be observed, even for the Sestak–Berggren equation, the best-fitting line exhibits large deviations when $\alpha \to 0$ and $\alpha \to 1$. These deviations are even larger in the case of the n-order kinetic model. Furthermore, the values of the squared correlation coefficient (R^2) (included in the figure legend) indicate that the fit is not acceptable, suggesting the need for proposing a new fitting equation. Thus, the following parametric function that is a hybrid between the zero-order kinetic model and an interface n-order reaction model is proposed:

$$f(\alpha) = 1 + \mu \left[(1 - \alpha)^n - \left(\frac{1}{2} \right)^n \right] \tag{24}$$

with two fitting parameters, μ and n. Note that $f(\alpha = 0.5) = 1$ regardless of the value of the fitting parameters. From now on, Eq. (24) is referred as generalized interface reaction
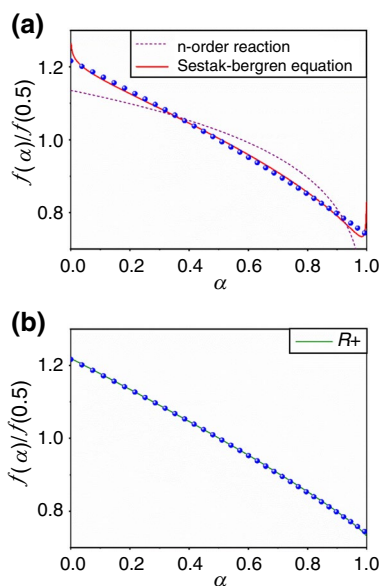
Fig. 6 **a** Fitting of the Sestak–Berggren and the n-order kinetic model to data plotted in Fig. 5b (dots) corresponding to a cuboid with edges $a_0 = 0.1$ μm, $b_0 = 0.5$ μm and $c_0 = 2$ μm and $k'' = 10^{-4}$ μm s^{-1}. For the Sestak–Berggren equation, the best-fitting parameters are: $C = 1.17$, $n = -0.22$, $m = 0.94$, $p = -0.95$ and $R^2 = 0.8889$. In the case of the n-order kinetic model: $A = 1.14$, $n = 0.15$ and $R^2 = 0.83604$. **b** Fitting of the $R+$ model to data plotted in Fig. 3b: $\mu = 0.49$, $n = 0.86$ and $R.^2 = 0.9999$

model ($R+$). Figure 6b shows the best fit of the $R+$ model to data plotted in Fig. 5b. The result is significantly better than those achieved with either the Sestak–Berggren equation or the n-order kinetic model (Fig. 6a), yielding a correlation coefficient very close to 1, which quantitatively demonstrates the high quality of the fitting.

The newly proposed generalized $R+$ model fits properly every interface kinetic model curve that has been tested. As a way of example, Table 1 collects the values of μ and n needed for reconstructing the curves represented in Fig. 3b, corresponding to cylindrical particles and two directions process progress, together with their corresponding squared correlation coefficients. As might be

Table 1 Values of μ and n needed for reconstructing the kinetic models plotted in Fig. 3b

ε	μ	n	R^2
0 (F0)	0	–	1
0.01	0.01999	0.99500	1
0.1	0.19816	0.95252	0.99998
1 (R3)	1.58740	0.66667	1
10	1.45601	0.57935	0.99992
100	1.41718	0.50926	1
$\varepsilon \rightarrow \infty$ (R2)	$\sqrt{2}$	0.5	1

observed, the $R+$ model adjusts the kinetic models curves with high accuracy, yielding very high correlation coefficients for all cases. Actually, in the case of the ideal R3 ($\varepsilon = 1$), R2 ($\varepsilon \rightarrow \infty$) and F0 ($\varepsilon = 0$) kinetic models, these correlation coefients have a value of 1. Figure 7 shows, as a way of example, the fitting for $\varepsilon = 10$, which represents the less favorable case according to the correlation coefficient obtained (Table 1). As shown in Fig. 7, even for this case, the $R+$ model properly fits the curve. Therefore, the $R+$ model can be used to describe the contraction of particles with different geometries including simple and complex cases.

Furthermore, real samples usually consist of particles with inhomogeneous particle size (broad distribution). To test the newly proposed $R+$ model for describing such complex situation, an isothermal curve has been simulated assuming that the sample is composed of cylindrical particles with the same radius but with an aspect ratio distribution given by lognormal function (Fig. 8a):
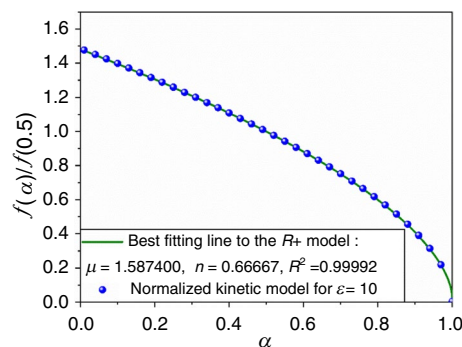
$$P(\varepsilon) = \frac{1}{\varepsilon\omega\sqrt{2\pi}}\exp\left(-\frac{(\ln\varepsilon - \omega)^2}{2v^2}\right) \qquad (25)$$

being ω and v the parameters that define the shape of the lognormal. For this sample, the total converted fraction can be expressed as follows:
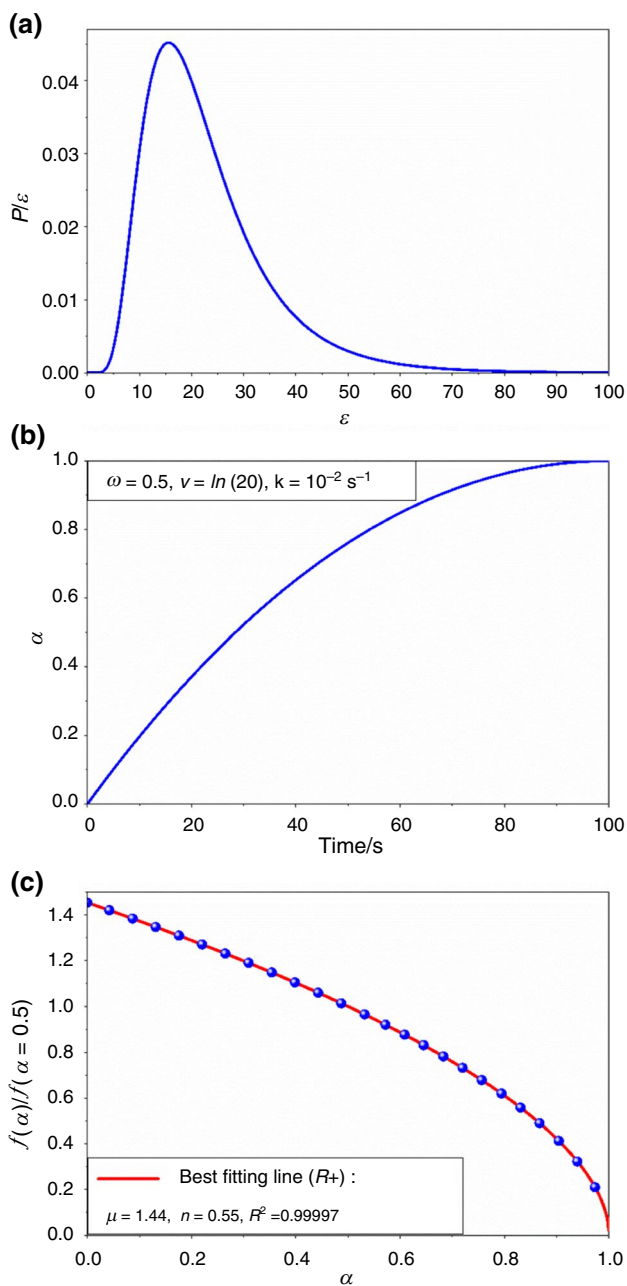
$$\alpha = \frac{\sum_\varepsilon \alpha_\varepsilon \varepsilon N_\varepsilon}{\sum_\varepsilon \varepsilon N_\varepsilon} \qquad (26)$$

where $N_\varepsilon = P(\varepsilon)\Delta\varepsilon$ and α_ε are the number of cylindrical particles with aspect ratio ε and its corresponding converted fraction, respectively. Therefore, taking into account Eq. (20), the converted fraction can be defined as follows:

$$\alpha(t) = \frac{\sum_\varepsilon \left[1 - (1 - kt)^2\left(1 - \frac{k}{\varepsilon}t\right)\right]\varepsilon P(\varepsilon)\Delta\varepsilon}{\sum_\varepsilon \varepsilon P(\varepsilon)\Delta\varepsilon} \qquad (27)$$


Fig. 7 Fitting of the $R+$ model to data simulated for $\varepsilon = 10$

(a)

(b)

$\omega = 0.5$, $v = ln(20)$, $k = 10^{-2}$ s^{-1}

(c)

Best fitting line ($R+$) :

$\mu = 1.44$, $n = 0.55$, $R^2 = 0.99997$

Fig. 8 a Lognormal-type aspect ratio distribution with $\omega = 0.5$ and $v = \ln(20)$. **b** Time evolution of the total converted fraction, simulated assuming a reaction constant of $k = 10^{-2}$ s^{-1}. **c** Normalized kinetic model and best-fitting line ($R+$ model) obtained: $\mu = 1.44$ and $n = 0.55$

Figure 8b shows the time evolution of α. The simulation was conducted assuming $\omega = 0.5$ and $v = \ln(20)$ for the aspect ratio distribution and a process rate of $k = 10^{-2}$ s^{-1}. The difference between two consecutive values of ε was $\Delta\varepsilon = 10^{-5}$. Figure 8c shows the normalized kinetic model calculated according to Eq. (24) and represented by dots. The best-fitting line using the $R+$ model has been plotted
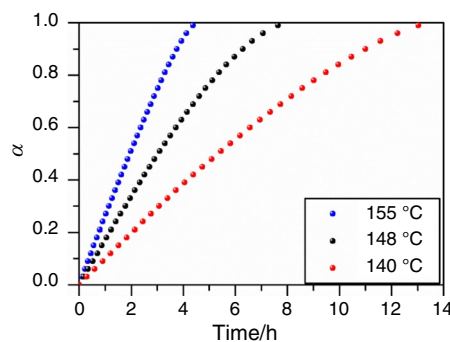
Fig. 9 Time evolution of α in the isothermal experiments conducted at 140, 148 and 155 °C

in the same graph as a continuous red line ($\mu = 1.44$ and $n = 0.55$). The value of $R^2 = 0.99997$ obtained demonstrates the capability of the proposed $R+$ model to describe the process. Therefore, the $R+$ generalized kinetic model proposed here can be used as an umbrella that cover complex contraction geometries and even the case of broad particle size distribution.

Experimental

Ammonium nitrate of 99.0% purity (Panreac) was used in this study. The experiments were conducted under both isothermal and linear heating rate conditions utilizing a thermogravimetric analyzer (TGA) Q650 from TA Instruments. Small amounts of sample ($\sim$ 3 mg) were used to minimize the heat and mass transfer phenomena. The isothermal curves were recorded at 140, 148 and 155 °C, with a flow rate of 100 mL min^{-1} of N_2. The experiments under linear heating conditions were carried out using a heating rate of 0.05 °C min^{-1} and two different gases, namely N_2 and Ar (100 mL·min^{-1}).

Kinetics of the thermal decomposition of ammonium nitrate

Figure 9 shows the time evolution of the converted fraction for the thermal decomposition of ammonium nitrate under isothermal conditions at 140 °C, 148 °C and 155 °C. These temperatures were selected below the melting point ($\sim$ 170 °C) to ensure that the decomposition takes place in the solid state. Actually, it has been reported in literature that under these conditions the process corresponds to sublimation [29].

Isothermal data are conventionally analyzed using a model-fitting procedure based on the integral form of the general kinetic equation for heterogeneous kinetics (Eq. 2).

Thus, the isothermal experimental curves are fitted with a set of different kinetic models, $g(\alpha)$, from literature to determine which one yields the best linearization of experimental data when $g(\alpha)$ is plotted as a function of time. Table 2 collects the integral form of some ideal kinetic models ranked according to the average squared correlation coefficient obtained in the linear fitting to $g(\alpha)$ versus time for the experimental data presented in Fig. 9.

The kinetic model $R2$ is the one with the highest value of R^2 and deserves special attention. Indeed, $R2$ has been previously identified as the model driving the thermal decomposition of ammonium nitrate, being the process described as a dissociative sublimation [29]. Nevertheless, the fitting of the experimental data (Fig. 9) to the $R2$ kinetic model (included in Fig. 10a) shows deviations for all three experimental curves.

Thus, it was considered of interest to test the $R+$ model for analyzing this process. Nonetheless, since the proposed kinetic model depends on the parameters μ and n, finding the general analytical expression for $g(\alpha)$ is non-trivial. Instead, the integral is approximated by a sum. Thus, the value of g at the instant $t = t_N$ is estimated by:

$$g\left(t = t_N, \mu, \gamma\right) = \sum_{i=0}^{N} \frac{\alpha\left(t_{i+1}\right) - \alpha\left(t_i\right)}{1 + \mu\left(\left(1 - \alpha\left(t_i\right)\right)^n - (0.5)^n\right)} \quad (28)$$

where N is the number of measurements up to the instant $t = t_N$, and $\alpha(t_i)$ is the converted fraction at $t = t_i$. Using the method described in detail in [40], the values of the parameters that best linearize g as a function of t were determined, finding $\mu = 2.08$, $n = 0.13$ and $<R^2> = 0.9999$. The results, plotted in Fig. 10b, demonstrate that $R+$ is more suitable for describing the sublimation process of ammonium nitrate than $R2$ (Fig. 10a). Figure 10c shows a comparison between the normalized kinetic models $R2$ and $R+$ considering $\mu = 2.08$, $n = 0.13$, as obtained from the kinetic analysis.

Table 2 Squared correlation coefficient obtained in the linear fitting to $g(\alpha)$ versus time for some ideal kinetic models from the literature

Kinetic model	$g(\alpha)$	$<R^2>$
Contracting area: $R2$	$1 - (1 - \alpha)^{1/2}$	0.9948
Zero-order: $F0$	α	0.9889
2D Avrami–Erofeev equation: $A2$	$[-\ln(1 - \alpha)]^{1/2}$	0.9853
Contracting volume: $R3$	$1 - (1 - \alpha)^{1/3}$	0.9801
3D Avrami–Erofeev equation: $A3$	$[-\ln(1 - \alpha)]^{1/3}$	0.9475
2D diffusion: $D2$	$(1 - \alpha)\ln(1 - \alpha) + \alpha$	0.9174
3D diffusion, Jander equation: $D3$	$\left(1 - (1 - \alpha)^{1/3}\right)^2$	0.7680
$R+$: $\mu = 2.08$ and $n = 0.13$	$1 + 2.08\left[(1 - \alpha)^{0.13} - (1/2)^{0.13}\right]$	0.9999

Fig. 10 **a** and **b**: $g(\alpha)$ as a function of time for the thermal decomposition of ammonium nitrate, and fittings to interface reaction kinetic model $R2$ and the proposed model ($R+$: $\mu = 2.08$, $n = 0.13$), respectively. **c** Normalized kinetic models: $R2$ and $R+$. **d** Determination of the pre-exponential factor and apparent activation energy from the Arrhenius plot
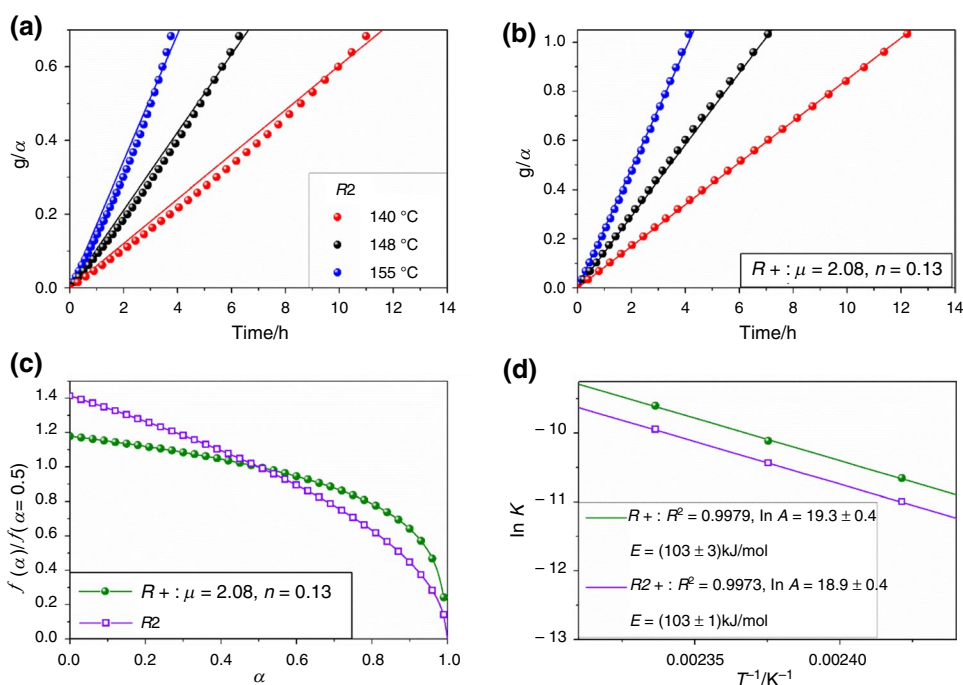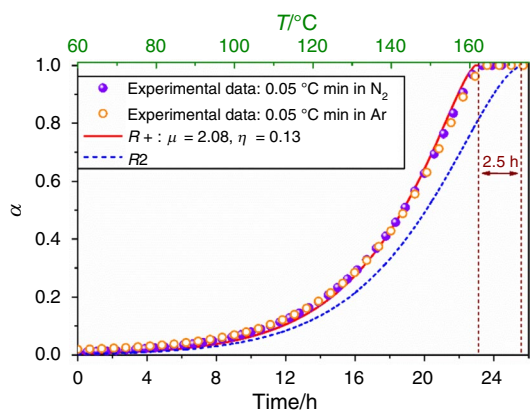
Fig. 11 Comparison between experimental data (for experiments conducted in N_2 and Ar) corresponding to the thermal decomposition of ammonium nitrate, and the curves simulated assuming linear heating conditions at 0.05 °C min^{-1} and using the two models compared in Fig. 10: $R2$ and $R+:\mu = 2.08, n = 0.13$

It should be highlighted that stablishing a direct correlation between the fitting parameters and the characteristics of the particle size distribution and the particle shapes is not straightforward and further research is necessary.

Values of rate constant, k, can be directly calculated from the slopes of the lines in Fig. 10a and b, as showed by Eq. (2). Moreover, the values of the pre-exponential factor and the apparent activation energy can be determined from the intercept and the slope, respectively, of the best-fitting line to the plot of $\ln k$ versus $1/T$ (Arrhenius plot):

$$\ln k = \ln A - \frac{E}{RT} \tag{29}$$

Figure 10d shows the Arrhenius plots for the two compared models. Albeit the value of the pre-exponential factor depends on the kinetic model, the apparent activation energy values coincide. Indeed, it has been previously demonstrated that the apparent activation energy determined from the kinetic analysis of isothermal data is independent of the model [41]. The determined value for the activation energy $E = (103 \pm 3)$ kJ mol^{-1} is in good agreement with those reported in the literature for this process [29].

Figure 11 shows a comparison between experimental data recorded under linear heating conditions at 0.05 °C min^{-1} and the predictions performed using the two models compared in Fig. 10 ($R+$ and $R2$), with their corresponding kinetic parameters. Previous studies on sublimation processes have pointed out gas diffusion in the solid–gas boundary as the rate-limiting step for low carrier gas flow rates [42, 43]. Nonetheless, the flow rate used in our experiments was high enough to discard this influence. To demonstrate this, two experiments were conducted using gases with different diffusion coefficients, namely N_2 and Ar. As may be seen in the figure, both experimental curves overlap showing

that gas diffusion does not play a significant role due to the high flow rates employed. The curves represented as continuous lines were simulated using the Runge–Kutta method with the conditions: $T(t = 0) = 50$ °C and $\alpha(t = 0) = 10^{-4}$. As might be observed, the prediction performed with $R+$ fits reasonably well the experimental data, while using the kinetic model $R2$ led to a difference of two and a half hours in the time prediction to reach full conversion ($\alpha = 1$). Therefore, Fig. 11 serves for validating the results of the kinetic analysis as the kinetic parameters could be used to properly predict the thermal behavior of the material even under heating conditions different from those used for the analysis. Furthermore, it illustrates that the correct selection of the kinetic model strongly compromises the predictions of the completion time of a process [44].

Conclusions

In this work, novel bidirectional and tridirectional contraction reaction mechanisms for particles that exhibit different geometries have been proposed. Thus, in the bidirectional case, it has been studied the contraction of cylinders with different aspect ratio, ε, values within a wide range $\varepsilon \in [0.01, 100]$. This is a general case that not only describes conventional contracting area kinetic models such as $R2$ ($\varepsilon \rightarrow 0$, a cylinder much longer than wide), $R3$ ($\varepsilon = 1$, sphere or cube) or $F0$ ($\varepsilon \rightarrow \infty$, contraction without change in reaction interface, traditionally associated with vaporization processes), but also many other possible realistic situations. Moreover, the contraction of rectangular cuboids has also been analyzed. In this latter case, dimensions of particles are different in the three directions of the space. Moreover, a novel generalized interface reaction model ($R+$) has been proposed, that not only covers all the studied cases but also it can be applied to more complex situations involving different geometries and inhomogeneous particle size distributions. The validation of the proposed model has been conducted through the analysis of the experimental thermal dissociation of ammonium nitrate in the solid state, which has been previously described as a sublimation process. Albeit the kinetics of the process resembles a contracting area model $R2$, the kinetic equation proposed here describes the reaction more accurately. Thus, although the apparent activation energy value determined here is in good agreement with those previously reported in the literature, the predictions capabilities of the newly proposed model are more accurate, as it has been demonstrated with experimental data.

References

1. Narnaware SL, Panwar NL. Kinetic study on pyrolysis of mustard stalk using thermogravimetric analysis. Bioresour Technol Rep. 2022;17: 100942. https://doi.org/10.1016/j.biteb.2021.100942.

2. Gaeini M, Shaik SA, Rindt CCM. Characterization of potassium carbonate salt hydrate for thermochemical energy storage in buildings. Energy Build. 2019;196:178–93. https://doi.org/10.1016/j.enbuild.2019.05.029.

3. El-Mesery HS, Farag HA, Kamel RM, Alshaer WG. Convective hot air drying of grapes: drying kinetics, mathematical modeling, energy, thermal analysis. J Therm Anal Calorim. 2023;148(14):6893–908. https://doi.org/10.1007/s10973-023-12195-0.

4. Hu J, Shan J, Zhao J, Tong Z. Isothermal curing kinetics of a flame retardant epoxy resin containing DOPO investigated by DSC and rheology. Thermochim Acta. 2016. https://doi.org/10.1016/j.tca.2016.02.010.

5. Menager C, Guigo N, Vincent L, Sbirrazzuoli N. Polymerization kinetic pathways of epoxidized linseed oil with aliphatic bio-based dicarboxylic acids. J Polym Sci. 2020;58(12):1717–27. https://doi.org/10.1002/pol.20200118.

6. Tziamtzi CK, Chrissafis K. Optimization of a commercial epoxy curing cycle via DSC data kinetics modelling and TTT plot construction. Polymer. 2021;230: 124091. https://doi.org/10.1016/j.polymer.2021.124091.

7. Vyazovkin S, Achilias D, Fernandez-Francos X, Galukhin A, Sbirrazzuoli N. ICTAC Kinetics Committee recommendations for analysis of thermal polymerization kinetics. Thermochim Acta. 2022. https://doi.org/10.1016/j.tca.2022.179243.

8. Zhang Y, Vyazovkin S. Comparative cure behavior of DGEBA and DGEBP with 4-nitro-1,2-phenylenediamine. Polymer. 2006;47(19):6659–63. https://doi.org/10.1016/j.polymer.2006.07.058.

9. Belioka MP, Siddiqui MN, Redhwi HH, Achilias DS. Thermal degradation kinetics of recycled biodegradable and non-biodegradable polymer blends either neat or in the presence of nanoparticles using the random chain-scission model. Thermochim Acta. 2023. https://doi.org/10.1016/j.tca.2023.179542.

10. Carrasco F, Pérez-Maqueda LA, Sánchez-Jiménez PE, Perejón A, Santana OO, Maspoch ML. Enhanced general analytical equation for the kinetics of the thermal degradation of poly(lactic acid) driven by random scission. Polym Test. 2013;32(5):937–45. https://doi.org/10.1016/j.polymertesting.2013.04.013.

11. Pérez-Maqueda LA, Sánchez-Jiménez PE, Criado JM. Evaluation of the integral methods for the kinetic study of thermally stimulated processes in polymer science. Polymer. 2005;46(9):2950–4. https://doi.org/10.1016/j.polymer.2005.02.061.

12. Yan QL, Zeman S, Sánchez Jiménez PE, Zhang TL, Pérez-Maqueda LA, Elbeih A. The mitigation effect of synthetic polymers on initiation reactivity of CL-20: physical models and chemical pathways of thermolysis. J Phys Chem C. 2014;118(40):22881–95. https://doi.org/10.1021/jp505955n.

13. Koga N, Favergeon L, Kodani S. Impact of atmospheric water vapor on the thermal decomposition of calcium hydroxide: a universal kinetic approach to a physico-geometrical consecutive reaction in solid–gas systems under different partial pressures of product gas. Phys Chem Chem Phys. 2019;21(22):11615–32. https://doi.org/10.1039/C9CP01327J.

14. Hara M, Okazaki T, Muravyev NV, Koga N. Physico-geometrical kinetic aspects of the thermal dehydration of trehalose dihydrate. J Phys Chem C. 2022;126(48):20423–36. https://doi.org/10.1021/acs.jpcc.2c07104.

15. Zhang J, Jiang L, Jin W, Yang G, Chen L, Lin Z. The hydration kinetics of cement pastes with deoxyribonucleic acid (DNA). J Therm Anal Calorim. 2023. https://doi.org/10.1007/s10973-023-12302-1.

16. Kremer I, Tomić T, Katančić Z, Erceg M, Papuga S, Parlov Vuković J, et al. Catalytic pyrolysis and kinetic study of real-world waste plastics: multi-layered and mixed resin types of plastics. Clean Technol Environ Policy. 2022;24(2):677–93. https://doi.org/10.1007/s10098-021-02196-8.

17. Matsui K, Hojo J. Initial sintering mechanism and additive effect in zirconia ceramics. J Am Ceram Soc. 2022;105(9):5519–42. https://doi.org/10.1111/jace.18484.

18. Pérez-Maqueda LA, Criado JM, Real C. Kinetics of the initial stage of sintering from shrinkage data: simultaneous determination of activation energy and kinetic model from a single nonisothermal experiment. J Am Ceram Soc. 2002;85(4):763–8. https://doi.org/10.1111/j.1151-2916.2002.tb00169.x.

19. Sun H, Zhang Y, Gong H, Li T, Li Q. Microwave sintering and kinetic analysis of Y_2O_3–MgO composites. Ceram Int. 2014;40(7 PART B):10211–5. https://doi.org/10.1016/j.ceramint.2014.02.106.

20. Gil-González E, Perejón A, Sánchez-Jiménez PE, Medina-Carrasco S, Kupčík J, Šubrt J, et al. Crystallization kinetics of nanocrystalline materials by combined X-ray diffraction and differential scanning calorimetry experiments. Cryst Growth Des. 2018;18(5):3107–16. https://doi.org/10.1021/acs.cgd.8b00241.

21. Honcová P, Valdés D, Barták J, Málek J, Pilný P, Slang S. Combination of indirect and direct approaches to the description of complex crystallization behavior in $GeSe_2$-rich region of pseudobinary $GeSe_2$–Sb_2Se_3 system. J Non-Cryst Solids. 2021. https://doi.org/10.1016/j.jnoncrysol.2021.120968.

22. Málek J, Svoboda R. Kinetic processes in amorphous materials revealed by thermal analysis: application to glassy selenium. Molecules (Basel, Switzerland). 2019. https://doi.org/10.3390/molecules24152725.

23. Shánělová J, Honcová P, Málek J, Perejón A, Pérez-Maqueda LA. Direct comparison of surface crystal growth kinetics in chalcogenide glass measured by microscopy and DSC. J Am Ceram Soc. 2023. https://doi.org/10.1111/jace.19204.

24. Soustelle M. Handbook of heterogenous kinetics. 2013. p. 1–28.

25. Vyazovkin S, Burnham AK, Criado JM, Pérez-Maqueda LA, Popescu C, Sbirrazzuoli N. ICTAC Kinetics Committee recommendations for performing kinetic computations on thermal analysis data. Thermochim Acta. 2011;520(1–2):1–19. https://doi.org/10.1016/j.tca.2011.03.034.

26. Koga N, Vyazovkin S, Burnham AK, Favergeon L, Muravyev NV, Pérez-Maqueda LA, et al. ICTAC Kinetics Committee

recommendations for analysis of thermal decomposition kinetics. Thermochim Acta. 2023;719: 179384. https://doi.org/10.1016/j.tca.2022.179384.

27. Ninan KN, Krishnan K, Krishnamurthy VN. Kinetics and mechanism of thermal decomposition of insitu generated calcium carbonate. J Therm Anal. 1991;37(7):1533–43. https://doi.org/10.1007/BF01913486.

28. Mamani V, Gutiérrez A, Ushak S. Development of low-cost inorganic salt hydrate as a thermochemical energy storage material. Sol Energy Mater Sol Cells. 2018;176:346–56. https://doi.org/10.1016/j.solmat.2017.10.021.

29. Vyazovkin S, Clawson JS, Wight CA. Thermal dissociation kinetics of solid and liquid ammonium nitrate. Chem Mater. 2001;13(3):960–6. https://doi.org/10.1021/cm000708c.

30. Buha J, Gaspari R, Del Rio Castillo AE, Bonaccorso F, Manna L. Thermal stability and anisotropic sublimation of two-dimensional colloidal Bi_2Te_3 and Bi_2Se_3 nanocrystals. Nano Lett. 2016;16(7):4217–23. https://doi.org/10.1021/acs.nanolett.6b01116.

31. Bales C, Gantenbein P, Jaenig D, Kerskes H, Summer K, Van Essen M et al. Laboratory tests of chemical reactions and prototype sorption storage units. 2008.

32. Koga N, Criado JM. Kinetic analyses of solid-state reactions with a particle-size distribution. J Am Ceram Soc. 1998;81(11):2901–9. https://doi.org/10.1111/j.1151-2916.1998.tb02712.x.

33. Arcenegui-Troya J, Sánchez-Jiménez PE, Perejón A, Pérez-Maqueda LA. Relevance of particle size distribution to kinetic analysis: the case of thermal dehydroxylation of kaolinite. Processes. 2021. https://doi.org/10.3390/pr9101852.

34. Šesták J, Berggren G. Study of the kinetics of the mechanism of solid-state reactions at increasing temperatures. Thermochim Acta. 1971;3(1):1–12. https://doi.org/10.1016/0040-6031(71)85051-7.

35. Pérez-Maqueda LA, Criado JM, Sánchez-Jiménez PE. Combined kinetic analysis of solid-state reactions: a powerful tool for the simultaneous determination of kinetic parameters and the kinetic model without previous assumptions on the reaction mechanism. J Phys Chem A. 2006;110(45):12456–62. https://doi.org/10.1021/jp064792g.

36. Gibson RL, Simmons MJH, Hugh Stitt E, West J, Wilkinson SK, Gallen RW. Kinetic modelling of thermal processes using a modified Sestak-Berggren equation. Chem Eng J. 2021;408: 127318. https://doi.org/10.1016/j.cej.2020.127318.

37. Hotta M, Tone T, Favergeon L, Koga N. Kinetic parameterization of the effects of atmospheric and self-generated carbon dioxide on the thermal decomposition of calcium carbonate. J Phys Chem C. 2022;126(18):7880–95. https://doi.org/10.1021/acs.jpcc.2c01922.

38. Sánchez-Jiménez PE, Perejón A, Criado JM, Diánez MJ, Pérez-Maqueda LA. Kinetic model for thermal dehydrochlorination of poly(vinyl chloride). Polymer. 2010;51(17):3998–4007. https://doi.org/10.1016/j.polymer.2010.06.020.

39. Khawam A, Flanagan DR. Solid-state kinetic models: basics and mathematical fundamentals. J Phys Chem B. 2006;110(35):17315–28. https://doi.org/10.1021/jp062746a.

40. Arcenegui-Troya J, Perejón A, Sánchez-Jiménez PE, Pérez-Maqueda LA. Flexible kinetic model determination of reactions in materials under isothermal conditions. Materials. 2023. https://doi.org/10.3390/ma16051851.

41. Arcenegui-Troya J, Sánchez-Jiménez PE, Perejón A, Pérez-Maqueda LA. Determination of the activation energy under isothermal conditions: revisited. J Therm Anal Calorim. 2023;148(4):1679–86. https://doi.org/10.1007/s10973-022-11728-3.

42. Karakaya C, Ricote S, Albin D, Sánchez-Cortezón E, Linares-Zea B, Kee RJ. Thermogravimetric analysis of $InCl_3$ sublimation at atmospheric pressure. Thermochim Acta. 2015;622:55–63. https://doi.org/10.1016/j.tca.2015.07.018.

43. Hikal WM, Weeks BL. Sublimation kinetics and diffusion coefficients of TNT, PETN, and RDX in air by thermogravimetry. Talanta. 2014;125:24–8. https://doi.org/10.1016/j.talanta.2014.02.074.

44. Sánchez-Jiménez PE, Perejón A, Arcenegui-Troya J, Pérez-Maqueda LA. Predictions of polymer thermal degradation: relevance of selecting the proper kinetic model. J Therm Anal Calorim. 2022;147(3):2335–41. https://doi.org/10.1007/s10973-021-10649-x.